UNIVERSITY OF LEEDS

This is a repository copy of *PersonalitySensing: A Multi-View Multi-Task Learning Approach for Personality Detection based on Smartphone Usage*.

White Rose Research Online URL for this paper:
http://eprints.whiterose.ac.uk/168960/

Version: Accepted Version

Proceedings Paper:
Gao, S, Li, W, Song, LJ orcid.org/0000-0002-0969-4091 et al. (3 more authors) (2020) PersonalitySensing: A Multi-View Multi-Task Learning Approach for Personality Detection based on Smartphone Usage. In: Proceedings of the 28th ACM International Conference on Multimedia. MM '20: The 28th ACM International Conference on Multimedia, 12-16 Oct 2020, Seattle, WA, USA. Association for Computing Machinery (ACM) , pp. 2862-2870. ISBN 9781450379885

https://doi.org/10.1145/3394171.3413591

© 2020 Copyright held by the owner/author(s). Publication rights licensed to ACM. This is the author's version of the work. It is posted here for your personal use. Not for redistribution. The definitive Version of Record was published in MM '20: Proceedings of the 28th ACM International Conference on Multimedia, http://dx.doi.org/10.1145/3394171.3413591

Reuse
Items deposited in White Rose Research Online are protected by copyright, with all rights reserved unless indicated otherwise. They may be downloaded and/or printed for private study, or other acts as permitted by national copyright laws. The publisher or other rights holders may allow further reproduction and re-use of the full text version. This is indicated by the licence information on the White Rose Research Online record for the item.

Takedown
If you consider content in White Rose Research Online to be in breach of UK law, please notify us by emailing eprints@whiterose.ac.uk including the URL of the record and the reason for the withdrawal request.

White Rose university consortium
Universities of Leeds, Sheffield & York

eprints@whiterose.ac.uk
https://eprints.whiterose.ac.uk/

Contents lists available at ScienceDirect

Journal of the European Ceramic Society

journal homepage: http://ees.elsevier.com

Original Article

New high temperature dielectrics: Bi-free tungsten bronze ceramics with stable permittivity over a very wide temperature range

Thomas Brown [a], Andy P. Brown [a], David. A. Hall [b], Thomas E. Hooper [a], Yizhe Li [b], Stuart Micklethwaite [a], Zabeada Aslam [a], Steven J. Milne [a,*]

[a] School of Chemical and Process Engineering, University of Leeds, Leeds, LS2 9JT, UK
[b] School of Materials, University of Manchester, Manchester, M13 9PL, UK

ABSTRACT

High relative permittivity, ε_r, over a very wide temperature range, -65 °C to 325 °C, is presented for ceramics designed to be compatible with base metal electrode multilayer capacitor manufacturing processes. We report a ≥ 300 °C potential Class II capacitor material free from Bi or Pb ions, developed by doping $Sr_2NaNb_5O_{15}$ with Ca^{2+},Y^{3+} and Zr^{4+} ions, according to the formulation $Sr_{2-2z}Ca_zY_zNaNb_{5-z}Zr_zO_{15}$. For sample composition z = 0.025, ε_r values are 1565 ± 15 % (1 kHz) from -65 °C to 325 °C. At a slightly higher level of doping, z = 0.05, ε_r values are 1310 ± 10 % from -65 °C to 300 °C. Values of the dielectric loss tangent, tanδ are ≤ 0.025 from −60 °C to 290 °C, for z = 0.025, with tanδ increasing to 0.035 at 325 °C. Microstructural analyses exclude core-shell mechanisms being responsible for the flattening of the ε_r –T response.

1. Introduction

Commercially available Class II high volumetric efficiency ceramic capacitors based on ferroelectric $BaTiO_3$ ceramics are specified from -55 °C to 125 °C – 175 °C for materials referred to by the Electronics Industries Alliance (EIA) codes as X7R-X9R (where R signifies stability in capacitance within ± 15 % of the room temperature value). For emerging power electronics applications relevant to the energy transition, an upper operating temperature ceiling of < 200 °C is insufficient [1]. High voltage power electronics for renewable energy generation and distribution require passive components that can operate alongside wide bandgap semiconductors at junction temperatures of 250 °C – 300 °C [2]. There are also a number of other applications where new Class II capacitors must maintain stable performance to ≥ 300 °C, for example distributed engine control systems for aerospace applications to reduce fuel consumption and improve reliability; and for drill-bit feedback systems in deep-well geothermal energy exploration [3]. Potential applications also arise in electric and hybrid vehicles.

In a bid to address these strategically important technological requirements, compositionally complex relaxor ferroelectrics with the perovskite ABO_3 crystal structure have been researched by many academic groups, recently with a focus on energy storage density measurements of multilayer samples [1–12]. Unfortunately, all of these materials contain bismuth oxide (or lead oxide). This prevents their application in base metal (Ni) electrode multilayer ceramic capacitors (MLCCs) – the main market. Bismuth or lead containing oxide ceramics are thermodynamically incompatible with metallic nickel electrode materials under the high temperature, chemically-reducing conditions used to co-fire base metal electrodes and the ceramic layers [13]. Hence most reports of MLCCs made with Bi or Pb containing ceramic dielectrics use expensive precious metal electrodes, at best Ag/Pd. The mainstream multilayer capacitor industry replaced precious metal electrodes with nickel, and to a lesser extent copper, many years ago on cost and security of supply consideration. For Bi-containing ceramic dielectrics co-fired with Cu there is a restricted processing window. Thermodynamic calculations indicate multilayers would have to be co-fired at temperatures <940 °C, and oxygen partial pressures, $Po_2 < 10^{-7}$ atm. [14]. By adding a series of liquid forming sintering fluxes to a $Na_{0.5}Bi_{0.5}TiO_3$ – based piezoceramic formulation, it proved possible to reduce the sintering temperature from 1150 °C to 900 °C, thereby enabling Cu electrodes to be demonstrated, but dielectric losses were higher than for samples fired in air [14]. A further issue or Bi- ceramic dielectrics relates to loss of volatile bismuth oxide during ceramic processing. Our interest in researching Pb, Bi-free high temperature dielectrics stems from industrial translation challenges of existing materials for applications in mass market Ni-electrode MLCCs.

* Corresponding author.
E-mail address: s.j.milne@leeds.ac.uk (S.J. Milne)

https://doi.org/10.1016/j.jeurceramsoc.2020.10.034
Received 21 May 2020; Received in revised form 12 October 2020; Accepted 19 October 2020
Available online xxx
0955-2219/© 2020.

UNCORRECTED PROOF

The best of the bismuth containing relaxor high temperature dielectrics are based on $Na_{0.5}Bi_{0.5}TiO_3$. For example, formulations in the $Na_{0.5}Bi_{0.5}TiO_3$-$Ba_{0.8}Ca_{0.2}Ti_{1-y}Zr_yO_3$-$NaNbO_3$ system developed in our laboratory have ε_r values of 1300 ± 15 % from -55 °C to 300 °C [8]. In other temperature-stable relaxors, such as (Ba,Ca)TiO_3-$BiMg_{0.5}Ti_{0.5}O_3$ or $BaTiO_3$-$BiZn_{0.5}Ti_{0.5}O_3$ solid solutions [7], the range of stable dielectric permittivity extends to upper temperatures exceeding 300 °C (~500 °C in some materials) but the lower limit is well above the Electronic Industries Appliance 'X' specified lower working temperature of -55 °C. Moreover, in many cases dielectric loss tangent values are relatively high, at least over part of the temperature span.

The need to discover alternative materials that avoid the use of heavy metal oxides so enabling integration with (Ni) base metal electrode MLCCs motivated us to shift the focus of research away from perovskite ferroelectrics. The criteria was to find a parent ferroelectric with dielectric anomalies at higher temperatures than for $BaTiO_3$ - the starting point for X7R capacitor materials. $BaTiO_3$ materials are limited to modest upper operating temperatures due to a Curie peak temperature of ~130 °C. Our criteria for designing new Bi-free next generation Class II dielectrics that could operate at significantly higher temperatures was to first select a parent ferroelectric with a higher Curie point, T_C, than $BaTiO_3$ *and* with a high $\varepsilon_{r\ max}$ value at T_C, such that even after compositionally engineering a suppression of the permittivity peak, high Class II levels of permittivity were retained over an extended temperature range. This led us to the tungsten bronze ferroelectric and non-linear optics literature. The material we selected, $Sr_4Na_2Nb_{10}O_{30}$, not only satisfied this selection criteria in terms of Curie point (305 °C) and $\varepsilon_{r\ max}$ value (~1400), it also displayed a second, lower temperature permittivity peak at -15 °C [15,16]. We considered that this would be of value in helping achieve stable permittivity to -55 °C, the EIA 'X' standard lower working temperature for a Class II capacitor. Relative permittivity varies by more than ± 20 % across the temperature range -55 °C to 300 °C for $Sr_4Na_2Nb_{10}O_{30}$.

The tungsten bronze crystal structure involves corner sharing of BO_6 octahedra in two crystallographic orientations (here B = Nb^{5+}) leaving three types of distinct crystallographic sites available for lower valence cations, labelled A2, A1 and C, in the generic formula $(A2)_4(A1)_2(C)_4(B1)_2(B2)_8O_{30}$ [15–21[32]], with co-ordination numbers 15, 12 and 9 for A2, A1 and C sites, respectively. The primary cell is tetragonal, but due to the existence of superstructures, either commensurate or incommensurate that involves modulation of the oxygen sublattice, the true symmetry may be orthorhombic with a much larger unit cell. A schematic of the tetragonal primary cell and its relationship to the larger orthorhombic unit cell is shown in Fig. 1. When viewed along the [001] direction, the A2 sites are visible as pentagonal channels, and the A2 square and C triangular channels. Our selection, $Sr_4Na_2Nb_{10}O_{30}$ is an example of a 'filled' tungsten bronze, so called because all A sites are occupied (although the C sites are empty). An early crystallographic study of a closely related tungsten bronze, $Ba_4Na_2Nb_{10}O_{30}$ was reported by researchers at Bell Telephone Laboratories [17]. However, $Sr_4Na_2Nb_{10}O_{30}$ is less widely reported, although some crystallographic information is available from a combination of X-ray and electron diffraction [15,16].

In $Sr_4Na_2Nb_{10}O_{30}$ tungsten bronze ferroelectrics a change from paraelectric to ferroelectric occurs with no change in crystal system: electrical properties may be strongly influenced by subtle changes to octahedral tilt systems, defect structures and crystal superstructures [15–21[32]]. Structure-property correlations have been less widely studied than for perovskite ferroelectrics and there is still much to learn. The results reported below will provide added stimulus for future wide-ranging studies to understand the fundamental structure-property relationships for this exciting new type of high temperature dielectric.

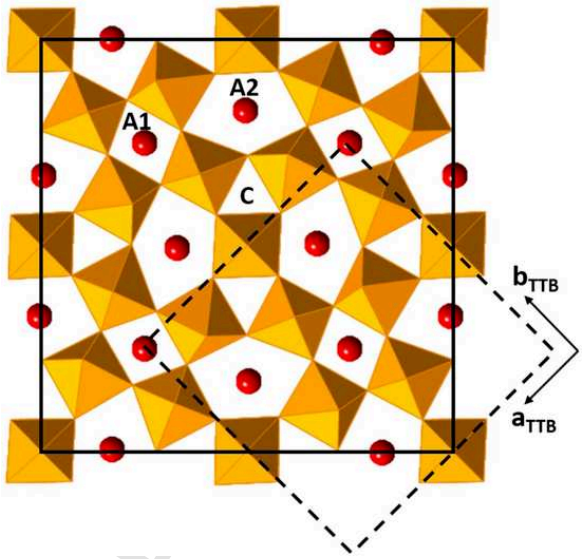

Fig. 1. Pseudocubic tetragonal primary cell of tungsten bronze structure (dashed lines) viewed along the [001] direction and its spatial relationship to a larger orthorhombic unit cell arising from by a superstructure (solid lines; after Ref [20]]. In $Sr_4Na_2Nb_{10}O_{30}$ Sr^{2+} and Na^+ ions are distributed over the A1 and A2 sites (red) formed by corner sharing NbO_6 octahedra (orange).

2. Experimental

For convenience, the chemical formula of the parent niobate phase ($Sr_4Na_2Nb_{10}O_{30}$) is expressed as $Sr_2NaNb_5O_{15}$ (SNN) in the remainder of the text. The substituted compositions are expressed assuming a solid solution formula $Sr_{2-2z}Ca_zY_zNaNb_{5-z}Zr_zO_{15}$. The assumption is that Ca^{2+} and Y^{3+} substituents will occupy A1/A2 sites and Zr^{4+} the Nb^{5+} (B) sites; C sites will remain empty. Sample formulations with z = 0, 0.025 and 0.05 were prepared using the mixed oxide route. The compositions correspond to a very low level of substitution. Only 1.25 at.% of the Sr^{2+} (A) sites are substituted by Y^{3+} in composition z = 0.025, and 2.5 at.% in z = 0.05. For B sites, the Zr^{4+} for Nb^{5+} levels are 0.5 at.% and 1 at.% for compositions z = 0.025 and 0.05 respectively.

Starting reagents of: strontium carbonate (Aldrich, 99.9 %); calcium carbonate (Aldrich, >99 %); sodium carbonate (Sigma-Aldrich, 99.95 %); niobium oxide (Alfa Aesar, 99.9 %); yttrium oxide (Alfa Aesar, 99.9 %) and zirconium oxide (Alfa Aesar, 99.7 %). Powders were mixed in appropriate ratios before ball-milling for up to 24 h in isopropanol using stabilised zirconia grinding media. Dried powders were calcined at 1200 °C for 6 h (heating rate 5 °C/min) in high purity alumina crucibles. The calcined powders with the addition of 2 wt.% of binder (Optapix AC112, Zschimmer & Schwarz) were ball milled in water for 24 h, dried and passed through a 300 μm mesh nylon sieve, before pressing uniaxially at 100 MPa (for 90 s) in a 1 cm diameter steel die. After uniaxial pressing, the green pellets were isopressed (200 MPa for 5 min) in an isostatic press (Stanstead fluid power, Essex, UK). Binder burn-out was performed at a heating rate of 1 °C/min to a dwell temperature of 550 °C and held for 5 h. Sintering was carried out after embedding the pellets in a powder of the same composition. Maximum densities were obtained at a sintering temperature of 1300 °C or 1350 °C; dwell times were 4–5 h. Sintered ceramic densities were measured from measured pellet dimensions and mass; the theoretical density was estimated from the nominal unit cell contents and measured lattice parameters.

Phase analysis by powder X-ray diffraction (XRD) was carried out using a Bruker D8 X-ray powder diffractometer. Unit cell lattice parameters of an adopted pseudo-tetragonal structure were obtained by full pattern Rietveld refinement using TOPAS 5.0 software (Bruker AXS,

UNCORRECTED

Karlsruhe, Germany). In the refinement analysis, the peak shape function was determined by the fundamental parameters of the X-ray diffractometer geometry. The refined parameters are background function coefficient, lattice constant, scale factor, and atomic coordination.

In order to prepare specimens for microstructural characterisation by scanning electron microscopy, ceramic pellets were mounted in epoxy resin (Epothin, Buehler) and ground with P240, P600 and P2500 silicon carbide paper. Subsequent sequential polishing was carried out using Texmet P microcloths with MetaDi 2 diamond suspensions of decreasing particle size: 9 μm, 3 μm and 1 μm. A final polish was carried out with ChemoMet and MasterMet 0.06 μm colloidal silica on a Buehler EcoMet 300 grinder/polisher. Chemical etching was carried out with a 2:1 ratio of hydrofluoric acid and concentrated nitric acid for 90 s at room temperature.

Scanning electron microscopy (SEM) was performed using a Hitachi SU8230 high performance cold field emission instrument fitted with an Oxford Instruments Aztec energy dispersive X-ray analysis (EDX) system with 80 mm^2 X-Max SD detector and analysis software. For transmission electron microscopy (TEM), thin sample lamellae were prepared via the in-situ lift-out method using a FEI Helios G4 CX Dual Beam - High resolution monochromated, field emission gun, scanning electron microscope (FEG-SEM) with precise Focused Ion Beam (FIB). In the Dual Beam microscope, 500 nm of platinum (Pt) was electron beam deposited (at 5 kV, 6.4 nA for the electron source) onto the surface of the target area. This was followed by a second Pt layer (1 μm) using the FIB (at 30 kV, 80 pA for the liquid Ga ion source). An initial lamella was cut (by the FIB at 30 kV, 47 nA), before a final cut-out was performed (at 30 kV, 79 nA). Final thinning and polishing of the lamellae to electron transparency was performed with a low energy ion beam (5 kV, 41 pA). The lamellae were attached, using ion beam deposited Pt onto a copper FIB lift-out grid (Omniprobe, USA) mounted within the SEM chamber (in-situ) ready for transfer to the TEM. The lamellae were imaged using a FEI Titan Themis^3 300 kV TEM fitted with a SuperX EDX system and Velox processing software.

For electrical measurements, silver electrodes were applied to opposite pellet faces (Sun Chemical, Gwent Electronic Materials). Relative permittivity, ε_r, and loss tangent, tanδ, were measured at low-field as a function of temperature at fixed frequencies using a Hewlett Packard HP4284 LCR analyser. An environmental chamber was used for lower temperatures down to -65 °C (TJR; Tenney Environmental-SPX, White Deer, CA). Ferroelectric hysteresis measurements were carried out using a HP33120A function generator in combination with a HVA1B high voltage amplifier (Chevin Research, Otley, UK), using a sinusoidal electric field waveform with a frequency of 2 Hz. The measured electric field-time and current-time waveforms were processed to yield polarisation-electric field (*P-E*) loops and effective complex permittivity values using the method described previously [23].

3. Results and discussion

Full-pattern refinements of X-ray powder diffraction data for crushed sintered pellets are shown in Fig. 2. Secondary phase $NaNbO_3$ was present in all three samples as has been reported by others for SNN [20,21]. In the present work, increasing the calcination and sintering times failed to eliminate the extra phase. Therefore, even for unmodified SNN the notional formula $Sr_2NaNb_5O_{15}$ may be inaccurate: for example, the Na rich secondary phase may be due to Sr^{2+} occupancy of a fraction of the perceived Na^+ sites, giving a formula $Sr_{2+x}Na_{1-2x}Nb_5O_{15}$ [24]. Monoclinic ZrO_2 secondary phase was identified only in the z = 0.05 sample. All phases were included in the Rietveld refinements.

We found no convincing evidence from XRD of weak extra superlattice reflections reported at around 20° 2θ or 37° 2θ which others have observed with the aid of electron diffraction, and attributed to an orthorhombic unit cell (Space Group Im2a). These reports relate to SNN samples which had been fabricated by sintering for 2 days at 1250 °C, followed by rapid quenching to room temperature [20]. Some workers have assigned SNN to a different orthorhombic space group, *Cmm*2 [25]. However the lack of any distinct supercell reflections in our XRD patterns prompted us to index on tetragonal axes, and to refine the data on the basis of space group *P4bm*. This tetragonal space group has been used in the past to index SNN samples obtained by calcining mixed oxide powders at 1150 °C for 12 h in an oxygen atmosphere [26]. The ambiguity in the literature as to space groups for SNN may in part relate to structural variations associated with different synthesis conditions. In a further example of the uncertainties in indexing diffraction patterns, a recent study of Ca^{2+} modified SNN reports a tetragonal phase for SNN with no Ca^{2+} substitution, changing to orthorhombic with increasing levels of Ca^{2+} substitution [24,27]. Verification of the true crystal system of SNN produced in our laboratory must await a detailed future study using electron and neutron diffraction. The emphasis of the present communication is to report microstructures and electrical properties of a new potential high temperature capacitor material.

Crystallographic data refined on *P4bm* are summarised in Table 1. The modifications by Ca^{2+}, Y^{3+}, Zr^{4+} produced a slight contraction in cell volume, consistent with solid solution formation.

Scanning electron micrographs of polished and etched sections of z = 0 and z = 0.05 are shown in Fig. 3. Observed grain sizes were similar (< 10 μm) for both compositions. Densities were 92–93 % of estimated theoretical values. The possibility of elemental segregation within the grains was investigated by SEM-EDX and TEM-EDX. For X7R $BaTiO_3$ based capacitor materials, a core-shell grain structure brought about by a variety of additive oxides is responsible for inducing a temperature stable permittivity response (from -55 °C to 125 °C). Thus it was important to establish if a comparable microstructure-strain mechanism was responsible for flattening the ε_r-T response of SNN. The SEM-EDX analysis for z = 0.05 showed no elemental gradation within grains, Fig. 4. The existence of secondary grains of sodium niobate and zirconia identified in XRD patterns (Fig. 1) with grain sizes of ~5 μm and ~1 μm respectively was confirmed by the SEM-EDX analysis; there was also some evidence from EDX for the presence of Sr in the sodium niobate grains. More detailed analysis using TEM-EDX confirmed an absence of core-shell grain structures, or indeed any form of elemental gradation within individual grains, Fig. 5.

The relative permittivity-temperature, ε_r-T response of the parent tungsten bronze $Sr_2NaNb_5O_{15}$ ceramic (SNN) is presented in Fig. 6a. The higher temperature dielectric peak at 305 °C is denoted T_2. For other tungsten bronzes, this dielectric anomaly is reported to correspond to the formation, on cooling, of a supercell which induces ferroelectric behaviour: hence T_2 represents the Curie point [16]. Structural correlations are less well understood in the context of the lower temperature dielectric peak T_1, which occurs at -14 °C in SNN (1 kHz) and shows frequency dispersion similar to a relaxor ferroelectric. An accompanying change in thermal expansion coefficient for related tungsten bronzes implies that the T_1 peak corresponds to a ferroelastic transition, but no associated structural deviations have been detected [18]. For z = 0 (SNN), the 'standard' dielectric peaks created a variation in ε_r of ± 22 % across the important temperature range, -55 °C to 300 °C, Fig. 6a. This is well outside the R-type ± 15 % stability level required of a Class II capacitor material. Consequently partial substitution of Sr^{2+} by Ca^{2+} was investigated for $Sr_{2-x}Ca_xNaNb_5O_{15}$ x < 0.1. The ε_r-*T* responses of SNN and Ca-SNN ceramics of comparable densities were generally similar. This finding is consistent with other reports [27]. Further chemical modifications, involving co-substitution of Ca^{2+}, Y^{3+} for Sr^{2+} and Zr^{4+} for Nb^{5+} were investigated in an attempt to supress the temperature variability in permittivity and attain R-type performance.

UNCORRECTED PROOF

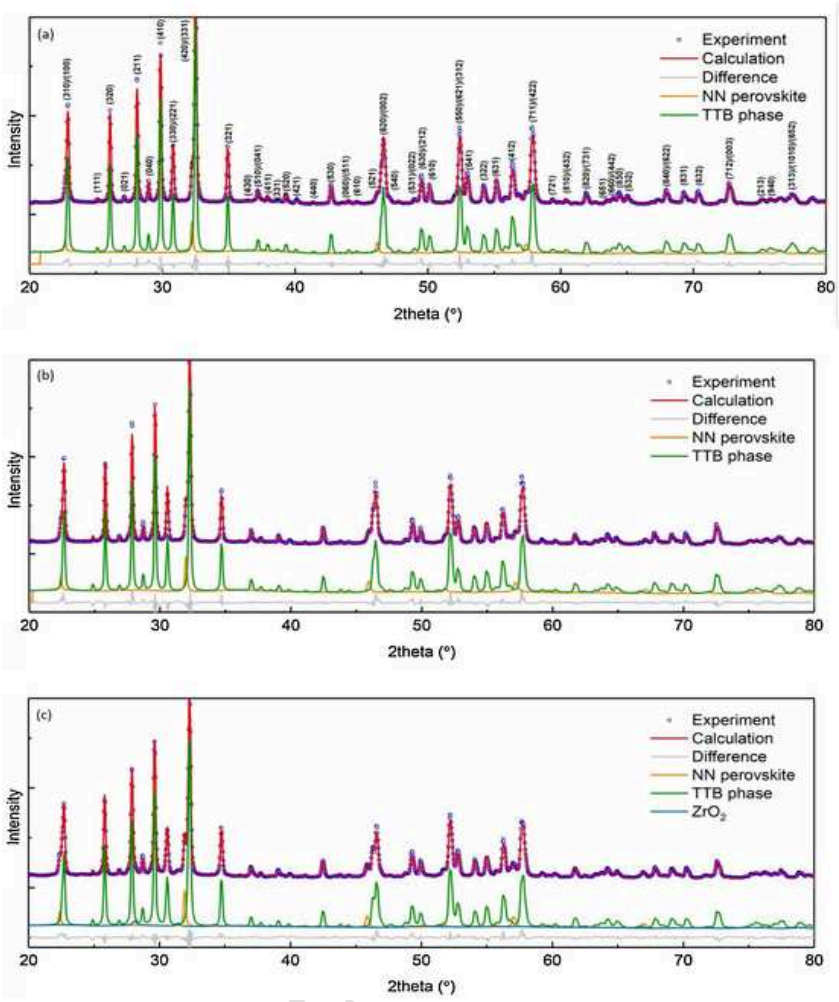

Fig. 2. Full pattern Rietveld refinements for $Sr_{2-2z}Ca_zY_zNaNb_{5-z}Zr_zO_{15}$: a) z = 0; b) z = 0.025; c) z = 0.05. The terms NN and TTB in the legends refer to a sodium niobate type perovskite secondary phase and the pseudo-tetragonal tungsten bronze main phase respectively.

Table 1
Summary of (pseudo) tetragonal lattice parameters, goodness of fit, R_{wp} and phase fractions from Rietveld analysis for $Sr_{2-2z}Ca_zY_zNaNb_{5-z}Zr_zO_{15}$.

Composition	a (Å)	c (Å)	V (Å ^{3})	R_{wp}%	%$NaNbO_3$
z = 0	12.365(90	3.8958(2)	595.73(3)	4.58	5.0
z = 0.025	12.362(9)	3.8920(1)	594.84(9)	4.99	7.4
z = 0.05	12.363(0)	3.8861(1)	593.97(3)	4.27	7.3 (+2.5 ZrO_2)

For the Ca^{2+},Y^{3+}, Zr^{4+} modified SNN sample composition z = 0.025, which had a very similar phase content to undoped SNN, the T_2 peak temperature increased to 345 °C, from a value of 305 °C in unmodified SNN (at 1 kHz); there was also a decline in the $\varepsilon_{r\ max}$ value due to increased broadening, Fig. 6b. For the lower temperature peak, there was very little change in peak temperature T_1 with substituent doping (−18 °C compared to −14 °C for SNN z = 0), but there was an increase in frequency dispersion. For sample composition z = 0.025 the difference in temperature, ΔT, of $\varepsilon_{r\ max}$ temperatures (T_m) between frequencies 1 kHz and 1 MHz was 25 °C, compared to 10 °C for unmodified SNN, z = 0.

For a higher level of chemical substitution, z = 0.05, the T_2 anomaly was now displaced to 255 °C, some 90 °C below the T_2 peak for z = 0.025, Fig. 6c. This non-monotonic shift of T_2 with z indicates a complex interplay between dopant level and temperature of the dielectric anomalies which may well relate to alterations in defect structures (possibly affecting NbO_6 tilts in the case of T_2). The T_2 anomaly also became significantly more diffuse as the level of substitution increased. As a result, the $\varepsilon_{r\ max}$ value at T_2 was approximately 60 % of that observed for unmodified SNN, z = 0. There was also an increase in broadening of the T_1 peak, Fig. 6c, but less so than for T_2. The presence of zirconia secondary phase in the microstructure may at least in-part account for the drop in $\varepsilon_{r\ 25°C}$ value compared to z = 0.025, but matrix strain effects consequent on transformation from tetragonal to monoclinic zirconia (on cooling from sintering temperatures) are thought unlikely, given the non-optimised sample density (92–93% theoretical).

The net effect of these chemical modifications on peak temperatures and peak profiles was to achieve the requisite ε_r ± 15 %, R-type consistency in ε_r over very wide ranges of temperature. For z = 0.025 the measured variation in the ε_r data was within ± 15 % of a median value of 1565 for temperatures extending from –65 °C to 325 °C (the median ε_r value occurred at ~105 °C). A further improvement in temperature-stability was achieved for higher levels of Ca^{2+}, Y^{3+} and Zr^{4+} substitution. The z = 0.05, sample composition gave a median value of ε_r = 1310 with a ± 10 % variation from temperatures of -65 °C to 300 °C. Very relevant to consideration as a capacitor material, the median value of ε_r in z = 0.05 ceramics occurred at 25 °C. Comparisons of

UNCORRECTED PROOF

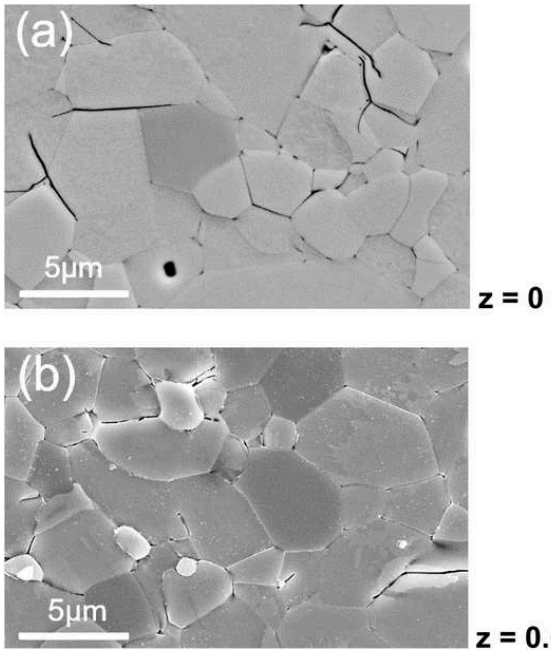

Fig. 3. SEM micrographs of $Sr_{2-2z}Ca_zY_zNaNb_{5-z}Zr_zO_{15}$: (a) z = 0 and (b) z = 0.05 (sintered for 4 h at 1300 ˚C).

the 1 kHz ε_r-T plots for z = 0, z = 0.025 and 0.05 are shown in Fig. 7 to highlight the development of temperature stable permittivity.

The low-field dielectric loss tangent values at 1 kHz were ≤ 0.035 from -65 ˚C to 320 ˚C (tanδ ≤ 0.025 from −60 ˚C to 290 ˚C) for z = 0.025. Losses were slightly higher in the z = 0.05 sample, with tanδ < 0.04. Dielectric data for these 92–93 % dense samples are summarised in Table 2.

Phase stability and electrical properties of SNN have been reported for only a limited number of other cation substitutions, and no specific discussion of temperature stability of permittivity has been presented. Substitution of Sb^{5+} for Nb^{5+} produced a change from orthorhombic *Ccm*2 to tetragonal *P*4*bm* Space Group, and shifted T_C to lower temperatures [28]. An evolution from orthorhombic to tetragonal crystal system was also induced by Eu^{3+}, and there was some indication from ε_r-T. The same research group also examined Sm^{3+} substitution in relation to thermal luminescent properties [29,30].

The P-E hysteresis loops for all of the compositions studied were generally similar in appearance and showed clear evidence of ferroelectric character, as illustrated in Fig. 8a. The maximum polarisation (initially around 13 μC.cm^{-2}) was reduced and the switching range around the coercive field became wider as z increased from 0 to 0.05. Significant dielectric nonlinearity and loss were evident in the sub-coercive field range, as illustrated in Fig. 8b. For example, the effective tanδ value at an electric field amplitude of 4 kV.cm^{-1} was determined as 0.154 for the undoped SNN, reducing to 0.081 and 0.060 for z = 0.025 and 0.05, respectively.

Nonlinearity was also apparent in the real and imaginary parts of the complex dielectric permittivity, as shown in Fig. 9. The observed behaviour generally departs from the classical Rayleigh Law (linear ε_r-E_{max} relation) [23], tending towards a quadratic response in the field range up to 15 kV.cm^{-1}. The degree of nonlinearity was strongly suppressed for z = 0.05, indicating reduced contributions to the electric field-induced polarisation from domain switching mechanisms, consistent with increasing disorder.

In summary, the primary dielectric parameters of Bi-free and Pb-free dielectric ceramics produced by very low levels of chemical substitution of a tungsten bronze $Sr_2NaNb_5O_{15}$ ferroelectric with Ca^{2+}, Y^{3+}, Zr^{4+} are class leading and very significant in the quest to develop base metal electrode Class II capacitor materials capable of operating over very wide temperature ranges. Future fundamental studies of crystal structure and defect chemistry will be required to elucidate the reasons why such low levels of compositional modification by Ca^{2+}, Y^{3+} and Zr^{4+} bring about such a dramatic change in the permittivity response. However, even at this early stage it is possible to exclude core-shell microstructural mechanisms, of the type which convert perovskite $BaTiO_3$ into a X7R temperature stable dielectric. Moreover, the concentrations of Ca^{2+}, Y^{3+}, Zr^{4+} required to flatten the permittivity response of SNN are far below those required to produce significant broadening of Curie peaks in perovskites due to compositional heterogeneity effects. It is anticipated that this first report of a novel high temperature dielectric with intriguing composition-property relationships will generate a range of follow-on research encompassing microstructural, compositional, phase stability and fundamental mechanistic studies.

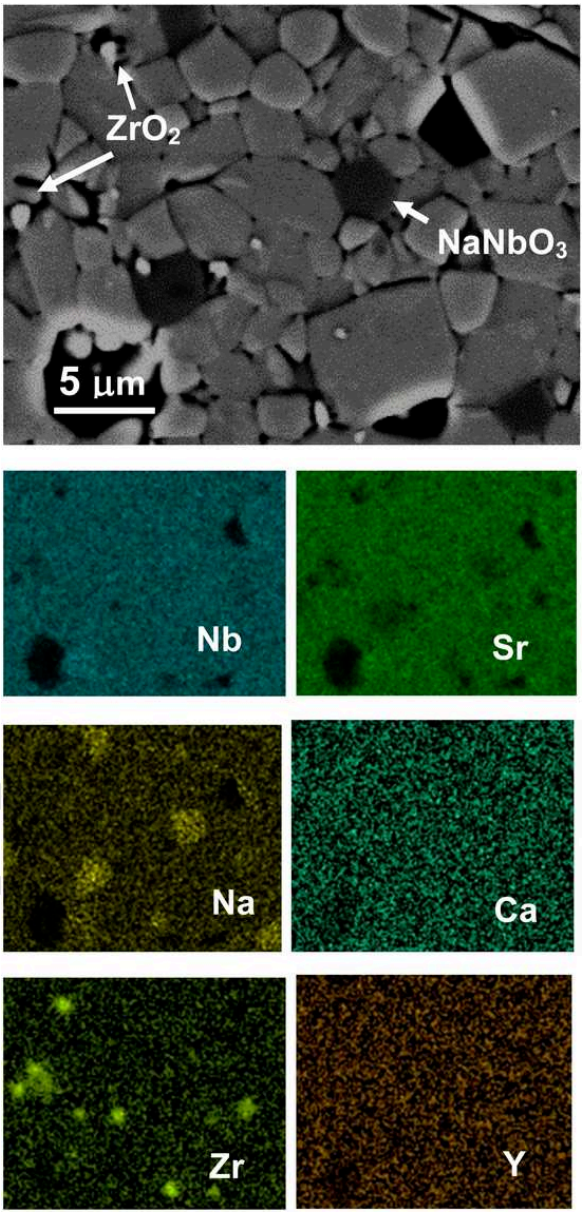

Fig. 4. SEM-EDX images of sample composition z = 0.05 showing a secondary Na-rich phase, consistent with the $NaNbO_3$ phase identified by XRD, and ZrO_2 grains (sintered at 1300 ˚C for 4 h).

UNCORRECTED

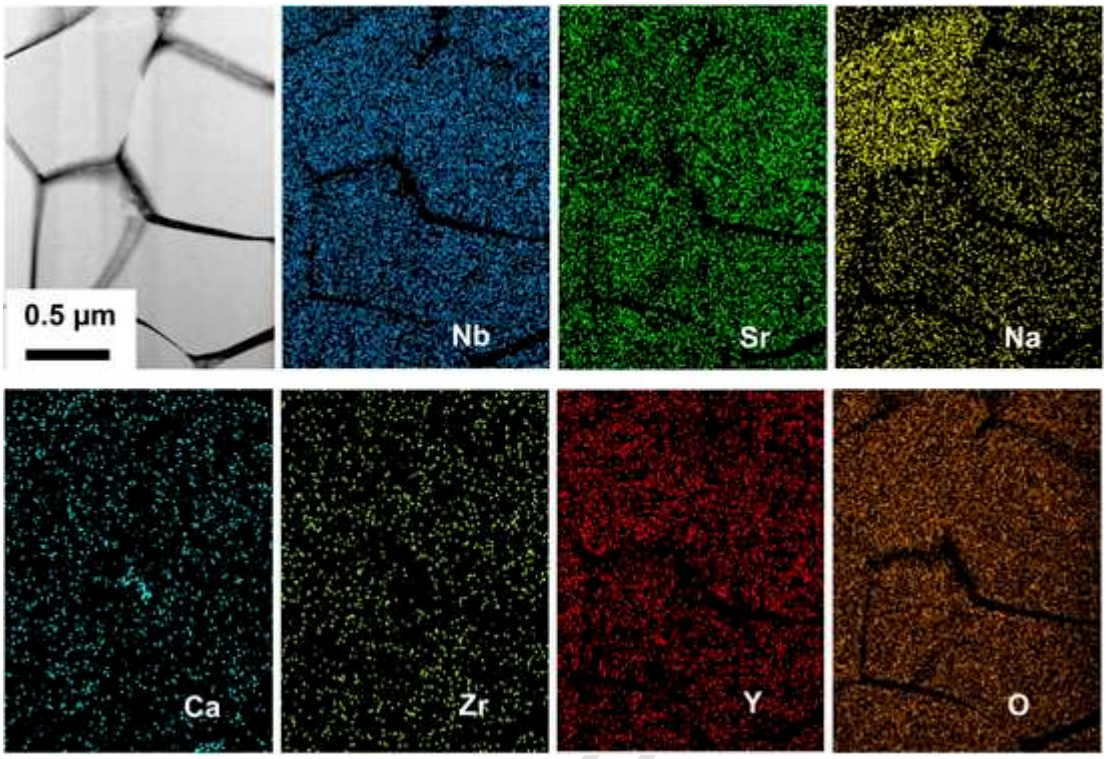

Fig. 5. Scanning TEM-EDX images confirming a lack of any detectable elemental gradation across grains - in contrast to conventional perovskite $BaTiO_3$ X7R temperature-stable dielectrics. Striations in HAADF* image (top left) are a 'curtaining' artefact of the FIB-SEM thinning method used to prepare the TEM specimen. * HAADF = high angle annular dark-field.

4. Conclusions

A high permittivity Class II ceramic dielectric that offers stable permittivity to > 300 ˚C and which does not contain problematic bismuth or lead oxides is demonstrated. Chemical substitution of $Sr_2NaNb_5O_{15}$ by Ca^{2+}, Y^{3+} and Zr^{4+} ions results in a material which more than satisfies the technologically important -55 ˚C to 300 ˚C temperature range of stable capacitance required for next generation power capacitor materials. For the formulation $Sr_{2-2z}Ca_zY_zNaNb_{5-z}Zr_zO_{15}$, z = 0.025, values of ε_r lie in the range 1565 ± 15 % for temperatures from -65 ˚C to 325 ˚C. At a higher dopant content, z = 0.05, the twin dielectric peaks become even more diffuse, giving ε_r values of 1310 ± 10 % from temperatures of -65 ˚C to 300 ˚C. Dielectric loss tangent values are ≤ 0.035 (1 kHz) across the full temperature range of stable permittivity for sample composition, z = 0.025, and tanδ ≤ 0.025 from −60 ˚C to 290 ˚C. Limiting dielectric losses were slightly higher, tanδ ≤ 0.04, for z = 0.05 samples. These primary dielectric properties are of high impact given the growing demands for next generation Class II capacitors that can operate at temperatures well beyond the limit of existing market-leading $BaTiO_3$ based capacitors (under 200 ˚C). The absence of any volatile bismuth oxide component is highly advantageous in the search for industrially-relevant dielectrics for future base metal electrode high temperature multilayer ceramic capacitors.

Declaration of Competing Interest

The authors declare that they have no known competing financial interests or personal relationships that could have appeared to influence the work reported in this paper.

Acknowledgements

S. J. Milne wishes to thank J. Bultitude, KEMET Electronics Corp. for invaluable background discussions on capacitor materials. A PhD scholarship for T. Brown was provided by School of Chemical and Process Engineering, University of Leeds.

Appendix A. Supplementary data

Supplementary material related to this article can be found, in the online version, at doi:https://doi.org/10.1016/j.jeurceramsoc.2020.10.034.

UNCORRECTED

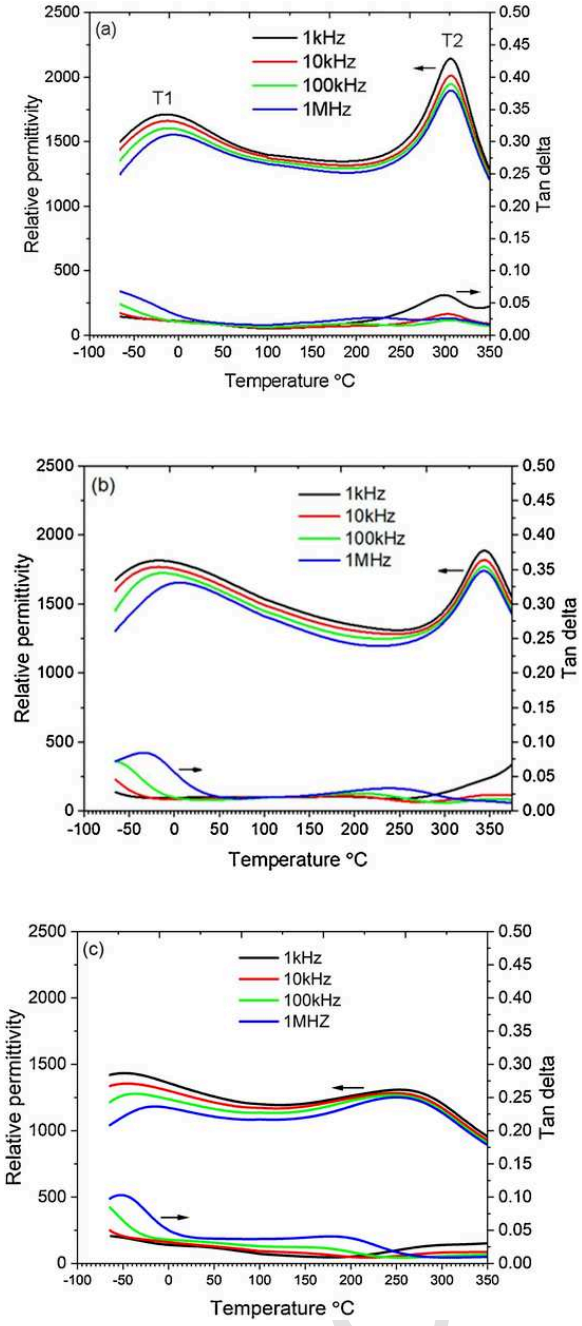

Fig. 6. Relative permittivity-temperature and loss tangent–temperature responses for $Sr_{2-2z}Ca_zY_zNaNb_{5-z}Zr_zO_{15}$: a) SNN z = 0; b) z = 0.025; c) z = 0.05.

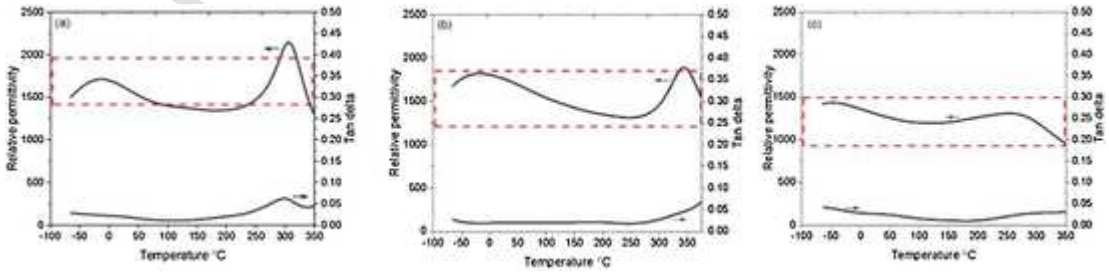

Fig. 7. Comparisons of the 1 kHz relative permittivity, highlighting the stability in ε_r values from -65 °C to ≥ 300 °C in $Sr_{2-2z}Ca_zY_zNaNb_{5-z}Zr_zO_{15}$: (a) z = 0; (b) z = 0.025; (c) z = 0.05. The dashed outline indicates the ± 15 % limits required by the EIA. Dielectric loss tangent plots are also shown.

Table 2
Summary of dielectric data of 92-93 % dense $Sr_{2-2z}Ca_zY_zNaNb_{5-z}Zr_zO_{15}$: ceramics (1 kHz data).

Sample Code	Intended Product Composition	ε_r median (T)	± % ε_r T range	*T* range tanδ ≤ 0.035	tanδ ≤ 0.03	tanδ ≤ 0.025
z = 0	$Sr_{2.0}Na_{1.0}Nb_{5.0}O_{15}$	1733 *(277 °C)*	22 % −65 °C to 300 °C	−65 °C to 249 °C	−65 °C to 238 °C	−32 °C to 223 °C
z = 0.025	$Sr_{1.95}C_{0.025}Na_{1.0}Y_{0.025}Zr_{0.025}Nb_{4.975}O_{15}$	1565 *(110 °C)*	15 % −65 °C to 325 °C	−65 °C to 320 °C	−65 °C to 310 °C	−60 °C to 290 °C
z = 0.05	$Sr_{1.90}Ca_{0.05}Na_{1.0}Y_{0.05}Zr_{0.05}Nb_{4.95}O_{15}$	1310 *(25 °C)*	10 % −65 °C to 300 °C	−40 °C to 370 °C*	−20 °C to 320 °C	+20 °C to 270 °C

*for z = 0.05, tanδ increased to 0.04 between -40 °C and –65 °C.

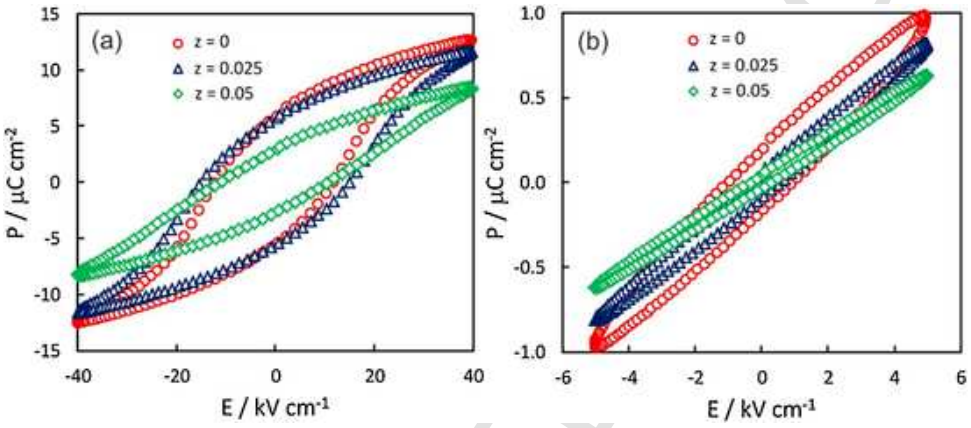

Fig. 8. Comparison of P-E loops for (a) E_{max} = 40 kV.cm^{-1} and (b) E_{max} = 5 kV.cm^{-1}.

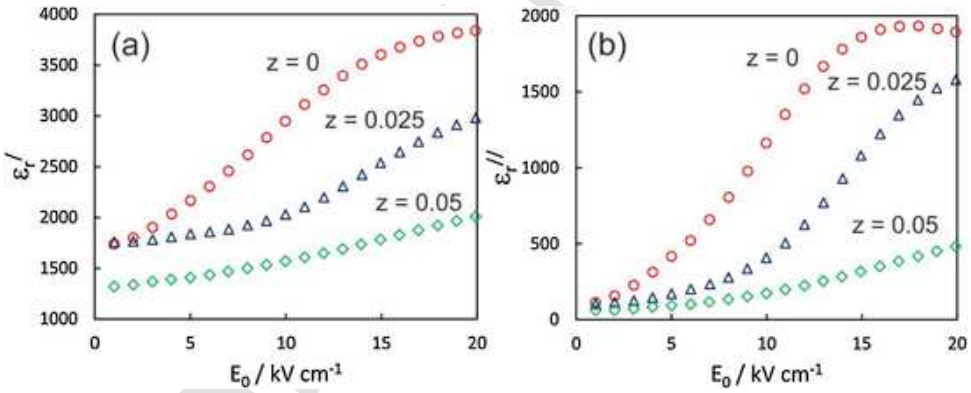

Fig. 9. Variations in (a) real and (b) imaginary parts of relative permittivity as a function of increasing electric field amplitude.

References

[1] J. Watson, G. Castro, A review of high-temperature electronics technology and applications, J. Mater. Sci. Mater. Electron. 26 (2015) 9226–9235, doi:10.1007/s10854-015-3459-4.

[2] Q. Li, F.-Z. Yao, Y. Liu, G. Zhang, H. Wang, Q. Wang, High-temperature dielectric materials for electrical energy storage, Annu. Rev. Mater. Res. 48 (3) (2018) 1–3, doi:10.1146/annurev-matsci-070317-124435.

[3] R. Phillips, J. Bultitude, A. Gurav, K. Park, S. Murillo, P. Flores, M. Laps, High temperature ceramic capacitors for deep Well applications, CARTS International, Proceedings, March 25-28, Houston, Texas, USA, 2013.

[4] R. Dittmer, W. Jo, D. Damjanovic, J. Rödel, Lead-free high-temperature dielectrics with wide operational range, J. Appl. Phys. 109 (2011) 034107, doi:10.1063/1.3544481.

[5] H. Ogihara, C.A. Randall, S. Trolier-McKinstry, High-energy density capacitors utilizing 0.7$BaTiO_3$–0.3$BiScO_3$ Ceramics, J. Am. Ceram. Soc. 92 (8) (2009) 1719–1724, doi:10.1111/j.1551-2916.2009.03104.x.

[6] H. Qi, R. Zuo, A. Xie, A. Tian, J. Fu, Y. Zhang, S. Zhang, Ultrahigh energy-storage density in $NaNbO_3$-based lead-free relaxor antiferroelectric ceramics with nanoscale domains, Adv. Funct. Mater. 19 (2019) 1903877, doi:10.1002/adfm.201903877.

[7] A. Zeb, S.J. Milne, Stability of high-temperature dielectric properties for (1−x)Ba0.8$Ca_{0.2}TiO_3$–xBi ($Mg_{0.5}Ti_{0.5}$)O_3 ceramics, J. Am. Ceram. Soc. 96 (9) (2013) 2887–2892, doi:10.1111/jace.12412.

[8] A. Zeb, S. Ullah Jan, F. Bamiduro, D.A. Hall, S.J. Milne, Temperature-stable dielectric ceramics based on Na0.5Bi0.5TiO_3, J. Eur. Ceram. Soc. 38 (4) (2018) 1548–1555, doi:10.1016/j.jeurceramsoc.2017.12.032.

[9] T. Roncal-Herrero, J. Harrington, A. Zeb, S.J. Milne, A.P. Brown, Nanoscale compositional segregation and suppression of polar coupling in a relaxor ferroelectric, Acta Mater. 158 (2018) 422–429, doi:10.1016/j.actamat.2018.07.053.

[10] G. Wang, J. Li, X. Zhang, Z. Fan, F. Yang, A. Feteira, D. Zhou, D.C. Sinclair, et al., Ultrahigh energy storage density lead-free multilayers by controlled electrical homogeneity, Energy Environ. Sci. 12 (2019) 582–588.

[11] Q. Xu, M.T. Lanagan, W. Luo, L. Zhang, J. Xie, H. Hao, M. Cao, Z. Yao, H. Liu, Electrical properties and relaxation behaviour of Bi0.5Na0.5TiO_3-$BaTiO_3$ ceramics modified with $NaNbO_3$, J. Eur. Ceram. Soc. 36 (10) (2016) 2469–2477, doi:10.1016/j.jeurceramsoc.2016.03.011.

[12] Q. Xu, Z. Song, W. Tang, H. Hao, L. Zhang, M. Appiah, M. Cao, Z. Yao, Z. He, H. Liu, Ultra-wide temperature stable dielectrics based on Bi0.5Na0.5TiO_3–$NaNbO_3$ system, J. Am. Ceram. Soc. 98 (10) (2015) 3119–3126, doi:10.1111/jace.13693.

[13] Y. Fang, M.T. Lanagan, D.K. Agrawal, G.Y. Yang, C.A. Randall, T.R. Shrout, A. Henderson, M. Randall, A. Tajuddin, An investigation demonstrating the

feasibility of microwave sintering of base-metal-electrode multilayer capacitors, J. Electroceramics 15 (2005) 13–19, doi:10.1007/s10832-005-0374-8.
[14] G. Yesner, A. Safari, Development of a lead-free copper co-fired BNT-based piezoceramic sintered at low temperature, J. Am. Ceram. Soc. 101 (2018) 5315–5322, doi:10.1111/jace.15777.
[15] E. García-González, A. Torres-Pardo, R. Jiménez, J.M. González-Calbet, Structural singularities in ferroelectric $Sr_2NaNb_5O_{15}$, Chem. Mater. 19 (14) (2007) 3575–3580, doi:10.1021/cm071303w.
[16] A. Torres-Pardo, R. Jiménez, J.M. González-Calbet, E. García-González, Structural effects behind the low temperature nonconventional relaxor behavior of the $Sr_2NaNb_5O_{15}$ bronze, Inorg. Chem. 50 (23) (2011) 12091–12098, doi:10.1021/ic2016098.
[17] P.B. Jamieson, S.C. Abrahams, J.L. Bernstein, Ferroelectric tungsten bronze-type crystal structures. I. Barium strontium niobate $Ba_{0.27}Sr_{0.75}Nb_2O_{5.78}$, J. Chem. Phys. 48 (1968) 5048, doi:10.1063/1.1668176.
[18] X. Zhu, M. Fu, M.C. Stennett, P.M. Vilarinho, I. Levin, C.A. Randall, J. Gardner, F.D. Morrison, I.M. Reaney, A crystal-chemical framework for relaxor versus normal ferroelectric behavior in tetragonal tungsten bronzes, Chem. Mater. 27 (9) (2015) 3250–3261, doi:10.1021/acs.chemmater.5b00072.
[19] I. Levin, M.C. Stennett, G.C. Miles, D.I. Woodward, A.R. West, I.M. Reaney, Coupling between octahedral tilting and ferroelectric order in tetragonal tungsten bronze-structured dielectrics, Appl. Phys. Lett. 89 (2006) 122908, doi:10.1063/1.2355434.
[20] J. Gardner, F.D. Morrison, A-site size effect in a family of unfilled ferroelectric tetragonal tungsten bronzes: $Ba_4R_{0.67}Nb_{10}O_{30}$ (R = La, Nd, Sm, Gd, Dy and Y), Dalton Trans. 43 (2014) 16887-11695, doi:10.1039/C4DT00126E.
[21] J.C. Toledano, L. Pateau, Differential thermal analysis of ferroelectric and ferroelastic transitions in barium sodium niobite, J. Appl. Phys. 45 (4) (1974) 1611, doi:10.1063/1.1663464.
[23] M. Stewart, M.G. Cain, D.A. Hall, Ferroelectric hysteresis measurement & analysis, National Physical Laboratory Report CMMT(A) 152 (1) (1999).
[24] B. Yang, J. Li, P. Yang, L. Wei, Z. Yang, Effects of A-site cations on the electrical behaviors in $(Sr_{1-x}Ca_x)_{2.1}Na_{0.8}Nb_5O_{15}$ tungsten bronze ferroelectrics, Mater. Chem. Phys. 243 (2020) 122006, doi:10.1016/j.matchemphys.2019.122006.
[25] J. Ravez, J.-P. Budin, P. Hagenmuller, Etude comparative des propriétés cristallographiques, diélectriques et d'optique non linéaire des phases $ABCNb5O_{15}$ (A = Ca, Sr, Ba, B = Ca, Sr, Ba, C = Na, K) de type "bronzes oxygénés de tungstène quadratiques", J. Solid State Chem. 5 (1972) 239, doi:10.1016/0022-4596(72)90034-5.
[26] S. Lanfredi, D.H.M. .Gênova, I.A.O. Brito, A.R.F. Lima, M.A.L. Nobre, Structural characterization and Curie temperature determination of a sodium strontium niobate ferroelectric nanostructured powder, J. Solid State Chem. 184 (2011) 990–1000, doi:10.1016/j.jssc.2011.03.001.
[27] L. Wei, Z. Yang, X. Han, Z. Hu, Structures, dielectric and ferroelectric properties of $Sr_{2-x}Ca_xNaNb_5O15$ lead-free ceramics, J. Mater. Res. 27 (2012) 979–984, doi:10.1557/jmr.2012.32.
[28] J. Fan, B. Yang, L. Wie, Z. Wang, B-cation effect on relaxor behavior and electric properties in $Sr_2NaNb_{5-x}Sb_xO_{15}$ tungsten bronze ceramics, Ceram. Int. 42 (3) (2016) 4054–4062, doi:10.1016/j.ceramint.2015.11.077.
[29] S. Hao, J. Li, P. Yang, L. Wei, Z. Yang, Enhanced electrical properties and strong red light-emitting in Eu^{3+}-doped $Sr1.90Ca_{0.15}Na_{0.9}Nb_5O_{15}$ ceramics, J. Am. Ceram. Soc. 100 (12) (2017) 5620–5628, doi:10.1111/jace.15085.
[30] S. Hao, J. Li, Q. Sung, L. Wei, Z. Yang, Improved electrical properties and good thermal luminescent stability of Sm^{3+}-doped $Sr_{1.90}Ca_{0.15}Na_{0.90}Nb_5O_{15}$ multifunctional ceramics, J. Mater. Sci. Mater. Electron. 30 (14) (2019) 13372–13380, doi:10.1007/s10854-019-01704-3.
[32] Lluis López-Conesa, Jose Rebled, Alicia Ruiz-Caridad, Almudena Torres-Pardo, Maria Luisa Ruiz-González, Jose González-Calbet, G. Dezanneau, Sonia Estradé, F. Peiró, Cation disorder in $Sr_{0.67}Ba_{0.33}Nb_2O_6$ assessed by aberration corrected stem, Results in Materials 3 (2019) 100038, doi:10.1016/j.rinma.2019.100038.

UNCORRECTED PROOF